



University of  
Massachusetts  
Amherst

## Discovery Of A Molecular Outflow In The Haro 6-10 Star-forming Region

Item Type	Article
Authors	Stojimirović, Irena;Narayanan, Gopal;Snell, Ronald L.
Download date	2025-06-27 09:09:24
Link to Item	<a href="https://hdl.handle.net/20.500.14394/2972">https://hdl.handle.net/20.500.14394/2972</a>

## DISCOVERY OF A MOLECULAR OUTFLOW IN THE HARO 6-10 STAR-FORMING REGION

IRENA STOJIMIROVIĆ<sup>1</sup>, GOPAL NARAYANAN, RONALD L. SNELL  
Astronomy Department, University of Massachusetts at Amherst, MA 01003  
*Draft version February 5, 2008*

### ABSTRACT

We present high sensitivity <sup>12</sup>CO and <sup>13</sup>CO J=1→0 molecular line maps covering the full extent of the parsec scale Haro 6-10 Herbig-Haro (HH) flow. We report the discovery of a molecular CO outflow along the axis of parsec-scale HH flow. Previous molecular studies missed the identification of the outflow probably due to their smaller mapping area and the confusing spectral features present towards the object. Our detailed molecular line study of the full 1.6 pc extent of the optical flow shows evidence for both blueshifted and redshifted gas set in motion by Haro 6-10 activity. The molecular outflow is centered at Haro 6-10, with redshifted gas being clumpy and directed towards the northeast, while blueshifted gas is in the southwest direction. The molecular gas terminates well within the cloud, short of the most distant HH objects of the optical flow. Contamination from an unrelated cloud along the same line of sight prevents a thorough study of the blueshifted outflow lobe and the mass distribution at the lowest velocities in both lobes. The cloud core in which Haro 6-10 is embedded is filamentary and flattened in the east-west direction. The total cloud mass is calculated from <sup>13</sup>CO J=1→0 to be ~ 200 M<sub>⊙</sub>. The lower limit of the mass associated with the outflow is ~ 0.25 M<sub>⊙</sub>.

*Subject headings:* ISM: clouds – ISM: jets and outflows – ISM:Herbig-Haro objects – individual Haro 6-10 – stars: formation

### 1. INTRODUCTION

In the last ten years, wide-field CCD camera observations have shown that it is quite common for outflows traced by Herbig-Haro (HH) objects to attain parsec scale dimensions, at least an order of magnitude larger than previously thought (Reipurth et al. 1997). It is now becoming clear that optical HH objects (which are lit up from the cooling behind shock fronts within the flows), near-infrared H<sub>2</sub> jets (tracing shocked regions), and the swept-up CO bipolar molecular outflows are intimately linked to one another (see for e.g. Bachiller et al. 1995). With the development of large-format heterodyne arrays at millimeter wavelengths and the availability of "on-the-fly" (OTF) mapping capabilities, millimeter mapping of the full extent of some of the known parsec-scale HH flows is possible with increased data sensitivity. This allows a more thorough study of the observational properties of the outflows and provides better constraints on the theoretical models of molecular outflow entrainment mechanism.

Devine et al. (1999) discovered a giant 1.6 pc long HH flow, centered on Haro 6-10 at a position angle of 222° delineated by HH 410 and HH 411 at its edges, and HH 412 and HH 184E along the HH flow axis. Haro 6-10 is located in the L 1524 cloud within the B18 region of the Taurus Molecular Cloud Complex. It is a binary system composed of an optically visible southern component (Haro 6-10S), and its infrared companion (Haro 6-10N). High-resolution 3.6 cm VLA map (Reipurth et al. 2004) strongly suggests that the optical component, Haro 6-10S, is driving the current outflow activity. The same set of data suggests that there might be an additional stellar companion to Haro 6-10S, more closely bound to

it than Haro 6-10N.

There has been other evidence for the outflow activity from the Haro 6-10 system such as 2.12 μm molecular hydrogen emission, observed at the position of the northern companion (Carr 1990; Herbst et al. 1995). Movsessian & Magakian (1999) found a small HH jet associated with Haro 6-10 itself at a position angle of 195° with blueshifted radial velocities. Reipurth et al. (2004) reported a VLA jet along the same angle. These latter jet angles are significantly different from the 222° angle of the parsec scale HH flow. The difference in these position angles have led some authors to suggest that the outflow from Haro 6-10 has undergone precession or reorientation (Reipurth et al. 2004; Devine et al. 1999). Devine et al. (1999) have argued that HH 184F-G and HH 184A-B are two different flows originating at the same time from two different protostars, probably due to an interaction in the binary pair. They have position angles of 162° and 231-249° respectively. HH 184E is the only knot in the HH 184 that is found along the parsec scale 222° axis and is the furthest away from driving source.

In the past, a few attempts have been made to detect molecular CO outflow from the Haro 6-10 source. Small maps, only a couple of arcminutes wide, have been made toward Haro 6-10 which presented the evidence of weak non-Gaussian CO wings emission in the direction of the optical object (Edwards & Snell 1984; Levreault 1988; Hogerheijde et al. 1997, 1998; Chandler et al. 1998). Hitherto, Haro 6-10 has been considered to be devoid of molecular outflow (Devine et al. 1999).

We made large, sensitive, <sup>12</sup>CO J=1→0 and <sup>13</sup>CO J=1→0 maps of the Haro 6-10 region, over the full extent of the optical parsec-scale HH flow. Here we show the evidence for the redshifted high velocity CO gas along the

<sup>1</sup> Current address: IAR, Boston University, Boston, MA,02215  
Electronic address: irena@bu.edu, gopal@astro.umass.edu, snell@astro.umass.edu

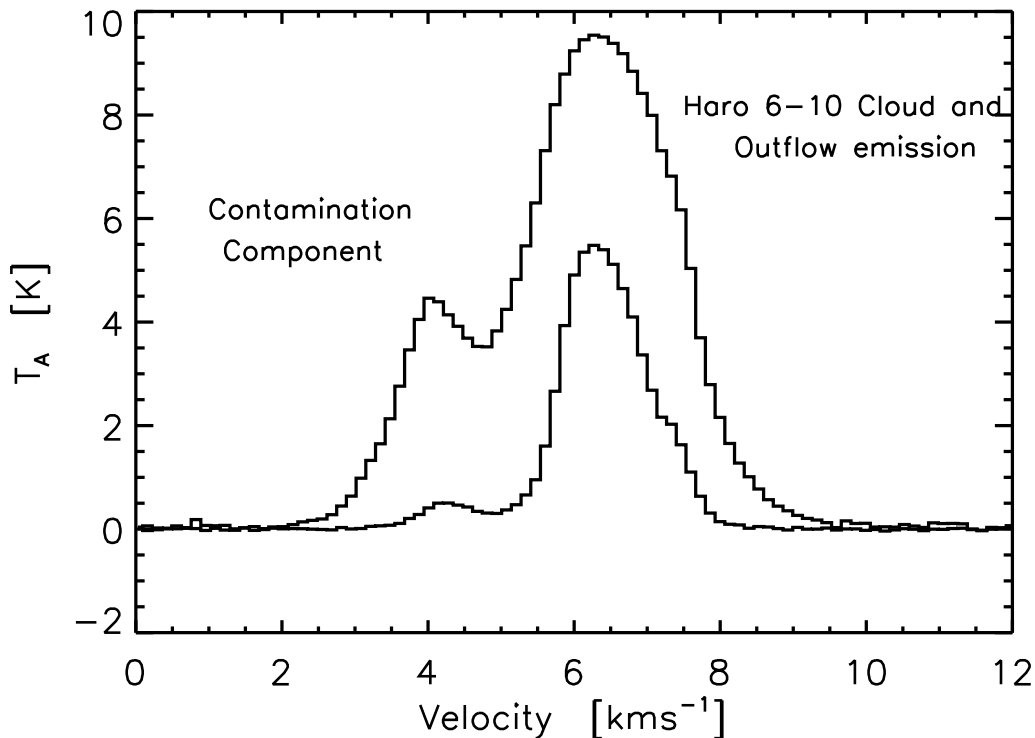


FIG. 1.— The  $^{12}\text{CO}$  and  $^{13}\text{CO}$  spectra averaged in  $15'$  area centered on Haro 6-10. Foreground contamination from another cloud in Taurus gives rise to the blueshifted emission peaking at  $\sim 4.5 \text{ km s}^{-1}$ .

FIG. 2.— (See f2.jpg) Overview of the Haro 6-10 region. A zoomed view into the B18 region derived from a much larger-scale map from the Taurus molecular cloud survey (Narayanan et al. 2007) in  $^{13}\text{CO } J=1\rightarrow 0$  (*a, b*) and  $^{12}\text{CO } J=1\rightarrow 0$  (*c, d*). These images demonstrate the presence of two emission components at different velocities, along the same line of sight. Panels *a* and *c* show emission unrelated to the B 18 cloud, while panels *b* and *d* trace the B 18 cloud sub-structure. In panel *b* we identify three clouds found in B 18: L 1529, L 1524, B18w, from east to west). Several YSOs and T-Tauri stars are embedded in the L 1529 region. L 1524 hosts Haro 6-10 star and nearby HH 414 IRS (filled stars). B 18w at the western most point, hosts IRAS 04239+2436 source which drives parsec scale HH 300 flow. In the panel *a* we label Haro 6-10 binary system, the driving source of parsec-scale HH flow with terminating points at HH 410 toward SW and HH 411 toward NE. Contours at each panel start at  $2\sigma$  level and go in steps of  $4\sigma$ .

to “contamination” by emission from another molecular cloud along the same line of sight, a thorough study of the blueshifted outflow lobe is limited.

## 2. OBSERVATIONS

A full mapping of  $^{12}\text{CO}$  and  $^{13}\text{CO}$  in the  $J=1\rightarrow 0$  transition was performed with the SEQUOIA receiver at the Five College Radio Astronomy Observatory (FCRAO) 14 m telescope during a period spanning 2003 and 2004. The receiver was configured as a dual-polarized  $4\times 4$  array. The orthogonal polarizations of the SEQUOIA array were averaged to produce spectra with higher signal-to-noise ratio (S/N). The telescope’s half-power beam widths are  $45''$  and  $47''$  for  $^{12}\text{CO}$  and  $^{13}\text{CO}$  transitions respectively. Channel maps as well as individual spectra were checked for any scanning artifacts, baselined and re-gridded to the  $22.5''$  sampled grid. RMS noise weighting was used to combine the data. For all calculations, the antenna temperatures were corrected for the main beam efficiencies of 0.45 for  $^{12}\text{CO}$  and 0.5 for  $^{13}\text{CO}$ .

Both  $^{12}\text{CO}$  and  $^{13}\text{CO}$  spectra are smoothed to  $0.13 \text{ km s}^{-1}$  channel spacing. The system temperatures ( $T_{sys}$ ) in our observations range from 400 – 700 K for  $^{12}\text{CO}$  and between 200 – 500 K for  $^{13}\text{CO}$ . Re-

gions mapped with the higher noise level were repeated, combined and averaged in order to get a constant lower noise level over the whole extent of the map. The resulting mean rms per velocity channel is  $0.2 \text{ K}$  for  $^{12}\text{CO}$  and  $0.1 \text{ K}$  for  $^{13}\text{CO}$ . Antenna pointing and focus were checked every few hours and corrected using SiO masers.

The analysis were done both using the Gildas software package and IDL software of Research Systems Inc. Detailed studies of the physical parameters characterizing the outflows were performed using IDL.

## 3. MORPHOLOGY OF THE CO GAS

### 3.1. Two component emission in B18 cloud

In Figure 1 we show  $^{12}\text{CO}$  and  $^{13}\text{CO}$  spectra averaged over a  $15'$  area centered on Haro 6-10. In both lines, the averaged spectra consists of two Gaussian-like components: a stronger component centered at  $6.4 \text{ km s}^{-1}$  and a weaker component at  $\sim 4 \text{ km s}^{-1}$ . A similar double peak profile has been observed by Arce & Goodman (2001, hereafter AG) by studying the parsec scale outflow from IRAS 04239+2426 in the adjacent B 18w cloud. They named the component at lower velocity “cloud A”, and surmised that it was produced by another cloud in Taurus along the same line of sight.

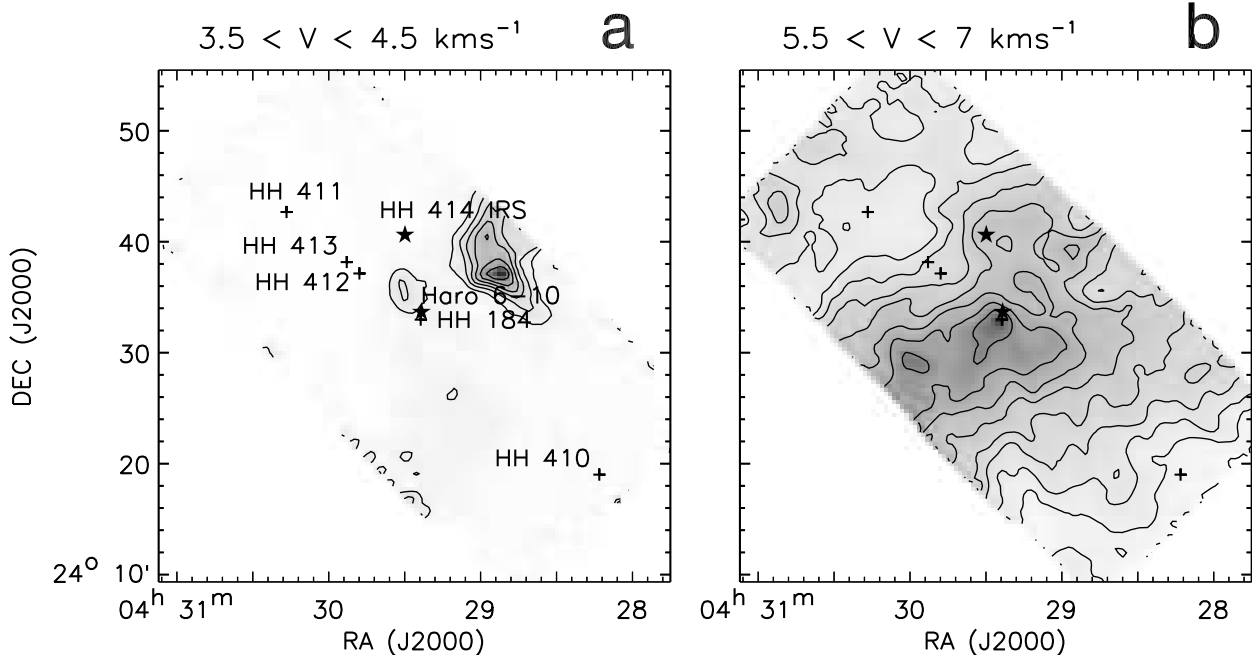


FIG. 3.— L 1524 cloud emission using our high sensitivity  $^{13}\text{CO}$   $J=1\rightarrow 0$  data integrated in two velocity bins, representing two distinct component in L 1524 cloud. Contours at each panel start at  $5\sigma$  level and go in steps of  $10\sigma$  in panel *a* ( $0.4\text{ Kkm s}^{-1}$ ) and in steps of  $20\sigma$  ( $0.9\text{ Kkm s}^{-1}$ ) in panel *b*. HH 184 coordinate is taken from Bo Reipurth’s General Catalog of HH Objects (<http://casa.colorado.edu/hhcat/>).

The stronger Gaussian component is associated with the Haro 6-10 host cloud, L 1524. This is in agreement with the ammonia core identified at LSR velocity of  $6.4\text{ km s}^{-1}$  (Codella et al. 1997) towards L 1524. Haro 6-10 is located at the edge of the compact ammonia core (see Figure 3, Codella et al. 1997). Our spatially averaged spectra towards the L 1524 cloud show some evidence for line wing emission at both blueshifted and redshifted velocities, although the contaminating cloud component at  $\sim 4\text{ km s}^{-1}$  obscures much of the wing emission at blueshifted velocities. Even with our higher sensitivity data, we do not see evidence for high velocity molecular gas as is seen in other prototypical outflows. Since the outflow is composed mainly of gas with slow radial velocities, emission from outflowing gas at the slowest velocities might be hidden under the ambient cloud emission.

In order to examine this contaminating emission at  $4\text{ km s}^{-1}$ , we used a  $2^\circ$  by  $2^\circ$  portion of the much larger FCRAO Taurus Molecular Cloud Survey in both  $^{12}\text{CO}$  and  $^{13}\text{CO}$   $J=1\rightarrow 0$  (Narayanan et al. 2007). In Figure 2, we plot for each line, the integrated intensity emission in two narrow velocity intervals. The first velocity interval preferentially selects the contaminating emission in the  $3.5$  to  $4.5\text{ km s}^{-1}$  velocity range, (Figure 2*a,c*). This contaminating cloud component is traced by  $^{13}\text{CO}$  molecule as an arc like filament, stretching from south of Haro 6-10 to north and appearing to bend toward IRS 04239+2436 in B18w cloud and south from it again, (see Figure 2*a*). The maximum intensity of this emission is south from IRS 04239+2436 source in the B 18w cloud, while at the location of Haro 6-10, the contaminating emission is quite clumpy. The  $^{12}\text{CO}$  tracer shows similar morphology of the emitting gas in the region (see Figure 2*c*).

In the other velocity interval, from  $5.5$  to  $7.0\text{ km s}^{-1}$  we preferentially select the CO emission associated with the B 18 clouds, which have LSR velocities around  $6.4\text{ km s}^{-1}$ . In  $^{13}\text{CO}$  (see Figure 2*b*), the B 18 cloud is revealed as a flattened, elongated structure in the east-west direction. In the same panel we identify L 1529, L 1524 and B 18w clouds within the B 18 region.

The dramatic change in the morphology for each isotope at only a slightly different velocity offset indicates quite clearly that we are looking at two spatially distinct and possibly unrelated cloud features. From Figure 2, it can be seen that towards Haro 6-10, the intensity of the contaminating emission is not as high as the intensity of the L 1524 cloud. However, towards B 18w, it is seen that the emission in both velocity bins seem to be of comparable intensity. The same was evident in the average spectra of the region presented by AG. In this study by AG, it was thus a clear cut in the case of IRAS 04239+2426 to concentrate only on the redshifted emission in the outflow. From the large-scale CO maps derived from the Taurus survey, it appears that while the blueshifted component in the Haro 6-10 spectra at  $4.5\text{ km s}^{-1}$  is part of the contaminating emission seen towards B 18w, the contamination is not nearly as severe as in the case of B 18w. Some of the emission towards Haro 6-10 at  $4.5\text{ km s}^{-1}$  might be part of the outflow system from that object.

### 3.2. The Haro 6-10 cloud core

In the following sections, we will examine in more detail the behavior of the ambient, blueshifted and redshifted gas using our new  $^{12}\text{CO}$  and  $^{13}\text{CO}$   $J=1\rightarrow 0$  data of Haro 6-10 outflow, which are of smaller scale compared to the Taurus survey, but have better sensitivity. For the rest of this paper, the Taurus Survey data are not used

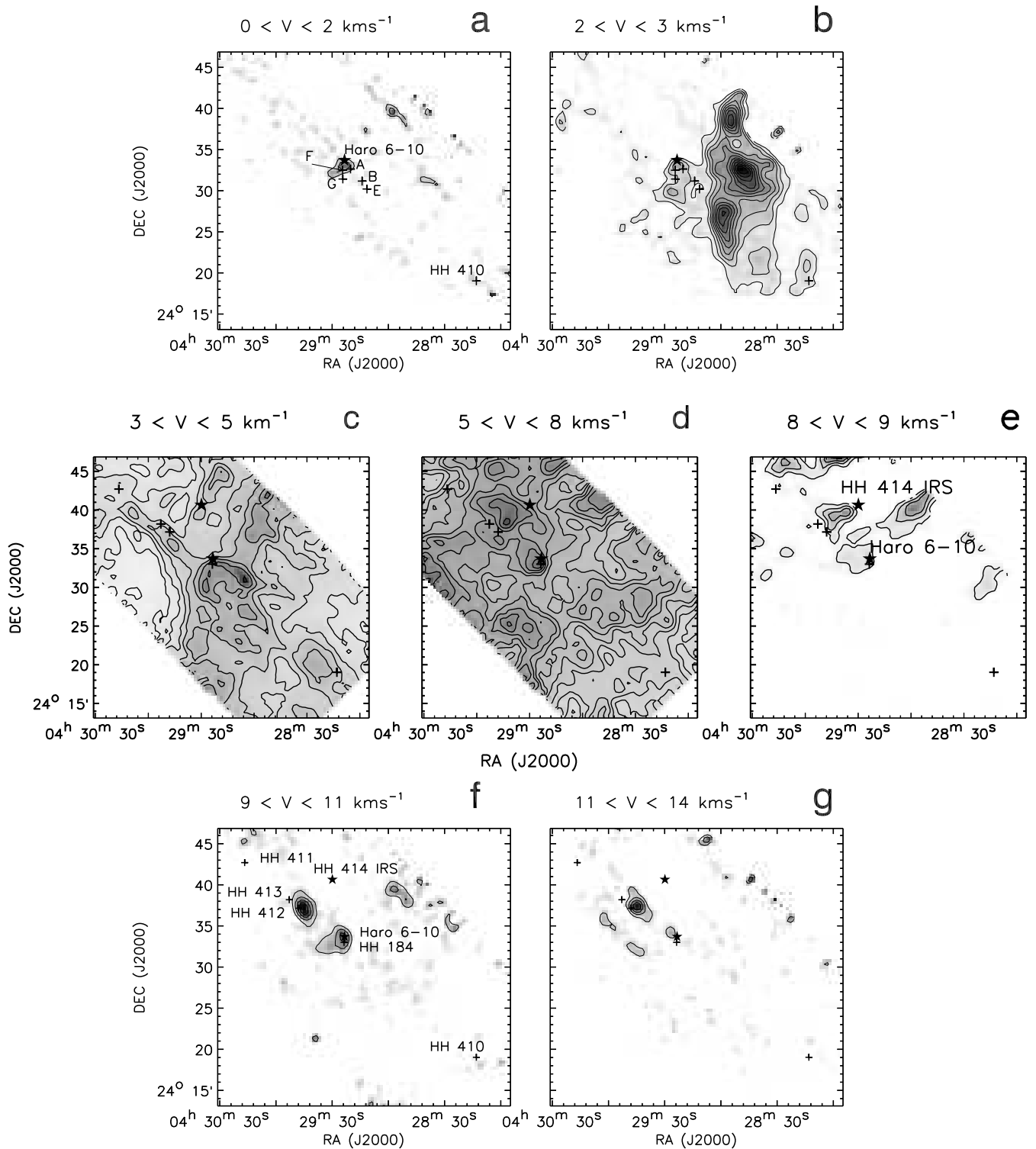


FIG. 4.—  $^{12}\text{CO}$  line integrated in different velocity intervals. Upper row: Blueshifted gas. In panel *a* contours start and increase with  $2\sigma$  certainty ( $2 \text{ K km s}^{-1}$ ), while in panel *b* they start and increase in  $3\sigma$  steps ( $2.1 \text{ K km s}^{-1}$ ). Middle row: Line Core. Contours in *c* and *d* panels start at  $10\sigma$  and go in step of  $10\sigma$  ( $1 \text{ K km s}^{-1}$  at panel *c* and  $1.2 \text{ K km s}^{-1}$  at panel *d*). In panel *e* contours start at  $8\sigma$  level ( $0.56 \text{ K km s}^{-1}$ ) and increase in the same step. Lower row: Redshifted gas. At both panels contours start and increase with  $2\sigma$  certainty, which is  $0.2 \text{ K km s}^{-1}$  in panel *f* and  $0.32 \text{ K km s}^{-1}$  in panel *g*. In *a*, *b* we mark different knots of HH 184 (Devine et al. 1999), while in the rest of the panels we use HH 184 coordinate as defined in Figure 3.

FIG. 5.— (See f5.jpg) Best case scenario for the outflow in the Haro 6-10 region: blueshifted emission is integrated in the velocity interval from 0 to 2 km s<sup>-1</sup> and contours start at 0.3 Kkm s<sup>-1</sup> and go in steps of 0.1 Kkm s<sup>-1</sup>; redshifted emission is integrated in velocity interval from 9 to 14 km s<sup>-1</sup> and contours start at 0.5 Kkm s<sup>-1</sup> and go in steps of 0.5 Kkm s<sup>-1</sup>. Molecular gas is overlaid on the optical image of the Haro 6-10 region (Devine et al. 1999) Again, we mark A, B, E, G knots of the HH 184 source (Devine et al. 1999).

for any analysis. As already discussed, in the velocity range between 3.5 and 4.5 km s<sup>-1</sup>, the emission is dominated by the contaminating cloud component. Figure 3 shows the <sup>13</sup>CO in two different velocity bins. Here, the contamination is clearly detected as strong feature at the northwest edge of the map (see Figure 3a). In addition, a small clump of emission centered at Haro 6-10 is present, which is elongated and extended toward north, at the ~ 30° angle with respect to the axis defined by the HH flow (crosses in Figures 3a). In the next panel, <sup>13</sup>CO emission traces the column density distribution within the L 1524 cloud. The flattened structure of the L 1524 cloud seen in the larger-scale map of Figure 2 is also visible here, and Haro 6-10 lies close to the peak of integrated intensity emission. This peak traces the same core identified in ammonia by Codella et al. (1997). The elongated L 1524 cloud is perpendicular to the HH outflow axis. From Haro 6-10, along the HH flow axis, the integrated intensity decreases, and HH 411 and HH 410 are found in the regions of very low <sup>13</sup>CO integrated intensity. The ridge of <sup>13</sup>CO emission is seen to extend northward from Haro 6-10 towards HH 414 IRS.

### 3.3. Outflow Emission

In Figure 4, we show integrated intensity emission of <sup>12</sup>CO in several different velocity bins. In the panels *a*, *f* and *g* we show the distribution of emission at the highest blueshifted and redshifted velocities. We believe that at these velocities we are selecting almost exclusively emission that arises from the outflow associated with Haro 6-10. Figure 4 *a* shows that the blueshifted emission in the velocity range from 0 to 2 km s<sup>-1</sup> is spatially restricted and centered on Haro 6-10. Compared to the bubble-like structures defined by the knots A-G of HH 184, the blueshifted emission has a smaller spatial extent and is elongated in the direction defined by A and F knots of HH 184. The spatial resolution of our data is such that it does not allow a more detailed comparison. In Figure 4 *f,g* the redshifted emission consists of two bright regions centered on Haro 6-10 and HH 412 respectively. The clump centered at Haro 6-10 has extended emission toward southeast, similar to the highest velocity blueshifted gas identified in Figure 4 *a*. The redshifted emission seen toward HH 412, located about 7' northeast of Haro 6-10, is detected to velocities as high as 14 km s<sup>-1</sup>, nearly 8 km s<sup>-1</sup> from the ambient cloud line center. The emission is slightly extended along the HH flow axis. In the optical images (Devine et al. 1999), HH 412 appears as a 1' long fairly diffuse emission feature, also elongated along the flow axis. Therefore, morphologies of the CO and optical emissions are quite similar around HH 412.

In Figure 5 we show the optical H $\alpha$  image of the Haro 6-10 region (Devine et al. 1999), overlaid with the <sup>12</sup>CO J=1 $\rightarrow$ 0 integrated emission in 9 to 14 km s<sup>-1</sup> velocity range for the redshifted gas and 0 to 2 km s<sup>-1</sup> for the blueshifted gas. In the optical image, HH 410 and HH 411, lie at the extremes of the HH flow, and are seen against a background with many galaxies, demonstrating that the flow has bursted out of the L 1524 cloud in

both directions, and is possibly now moving through a region with greatly reduced column density. Our <sup>13</sup>CO maps with negligible emission in these regions support this hypothesis. The expanded image of the CO outflow in Figure 5 shows that even toward Haro 6-10, the redshifted and blueshifted outflowing gas are slightly offset, suggesting that the outflow is bipolar with the redshifted emission to the northeast and blueshifted emission to the southwest. Devine et al. (1999) speculated, based on morphology and brightness, that the large HH flow has the same bipolar orientation. Additional information is provided by the radial velocity measurement of the small HH jet oriented at position angle 195° that shows that it is blueshifted (Movsessian & Magakian 1999), and thus has the same velocity sense at the CO outflow, although the jet is oriented about 30° from the large HH flow.

The distribution of CO emission in the near outflow wings, 2 to 3 km s<sup>-1</sup> for the blueshifted gas and 8 to 9 km s<sup>-1</sup> for the redshifted gas, is shown in Figure 4 *b,e*. On the blueshifted side, emission is seen toward Haro 6-10 (as in Figure 4 *a*) along with much brighter and very extended emission oriented in a north-south direction. The southern most part of this emission lies on the HH flow axis and may be associated with the flow. However, most of the emission presumably has nothing to do with the flow. Therefore the emission in the 2 to 3 km s<sup>-1</sup> range may be a mix of emission from the contaminating gas component as well as emission from the outflow. It is interesting to note that at these velocities the CO emission close to Haro 6-10 is extended in the direction toward knots F and G in HH 184. Because of the contamination in this velocity interval we can not be sure whether this is outflow related or unrelated emission. Likewise in the 8 to 9 km s<sup>-1</sup> range there is emission near Haro 6-10 that may be related to the CO outflow. An additional feature is found to the north-east of Haro 6-10 and connects HH 414 IRS to HH 413 and HH 412. Devine et al. (1999) detected a small jet originating from HH 414 IRS (IRAS 04264+2433) that was directed toward HH 413. They also suggested that the morphology of HH 413 knots resembled bow shocks originating from the direction of HH 414 IRS. The morphology of the CO emission is suggestive that it is tracing the molecular counterpart to the HH 414 IRS flow. There could be also some contamination at these velocities from the overall Haro 6-10 flow oriented north-east to south-west. It is noteworthy that the outflow axis, defined by the HH 414/413 optical flow and by the CO emission connecting them, is nearly perpendicular to the axis of the main parsec-scale HH outflow. Bright CO emission is also seen north-west of Haro 6-10 that is presumably unrelated to either flow. Again the emission in this velocity range is likely a mix of outflow emission and emission from the ambient gas.

Finally it is interesting to note the structure in the 3 to 5 km s<sup>-1</sup> interval, Figure 4 *c*. This velocity interval would be expected to include the outflow emission from Haro 6-10, since it lies a few km s<sup>-1</sup> from the line center of the L1524 cloud emission, however the second cloud contaminates the emission. It is intriguing that there

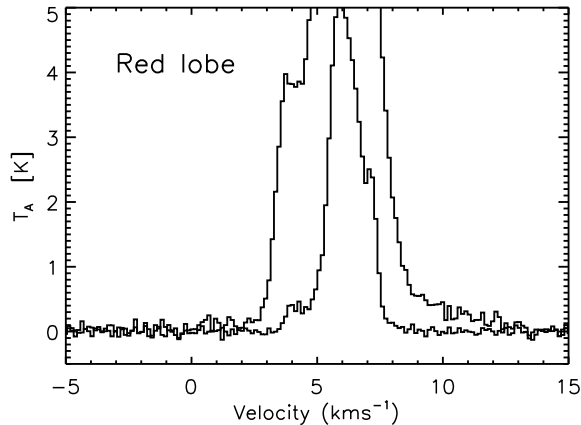


FIG. 6.—  $^{12}\text{CO}$  (thick) and  $^{13}\text{CO}$  (thin) spectra averaged in the redshifted lobe of the Haro 6-10 outflow.

a finger-like emission from Haro 6-10 toward the northeast, and a bow shaped feature centered on Haro 6-10, and opening toward HH 410 in the southwest. These two features line up with the HH flow direction. The relevance of this structure to the outflow is unclear. In the following velocity bin (5 to 8  $\text{km s}^{-1}$ ), the  $^{12}\text{CO}$  emission is dominated by L 1524 ambient cloud emission and no clear structure can be identified, although there is a maximum of emission towards Haro 6-10.

#### 4. MASS AND ENERGETICS

The emission from  $^{13}\text{CO}$  is usually optically thin and therefore a good tracer of the gas column density. However, the emission can also be very weak, limiting the spatial and velocity extent to which outflows can be traced. While  $^{12}\text{CO}$  is more readily detected, it is often optically thick, even in the high velocity emission of outflows. To derive accurate gas column densities we may need to correct for the optical depth of this line. Several recent studies have combined  $^{12}\text{CO}$  and  $^{13}\text{CO}$   $J=1\rightarrow 0$  data to estimate the mass of the outflow, using a velocity-dependent opacity correction (Bally et al. 1999; Yu et al. 1999; Arce & Goodman 2001; Stojimirović et al. 2006). This approach usually requires construction of spatially averaged spectra, since  $^{13}\text{CO}$  emission is usually not detectable in most mapping positions. The application of this method in Haro 6-10 has some limitations due to the weak emission in the line wings.

##### 4.1. Outflow Mass

In Figures 6 and 7 we show the spatially averaged  $^{12}\text{CO}$  and  $^{13}\text{CO}$  spectra in the redshifted and blueshifted gas respectively. These spectra were constructed using the following procedure to isolate the strongest outflow emission. For the blueshifted gas we found the integrated intensity at each location in our  $^{12}\text{CO}$  map in the velocity range from 0 to 2  $\text{km s}^{-1}$ . We then averaged the spectra at every location where the integrated intensity of  $^{12}\text{CO}$  was at least one-third of the peak integrated intensity. The  $^{13}\text{CO}$  spectrum was obtained by averaging the same spatial locations as was used to form the  $^{12}\text{CO}$  spectrum. For the redshifted gas we applied the same approach integrating over the velocity range of 9 to 12  $\text{km s}^{-1}$ . The resulting spectra differ from the average spectrum shown in Figure 1 in having both a weaker

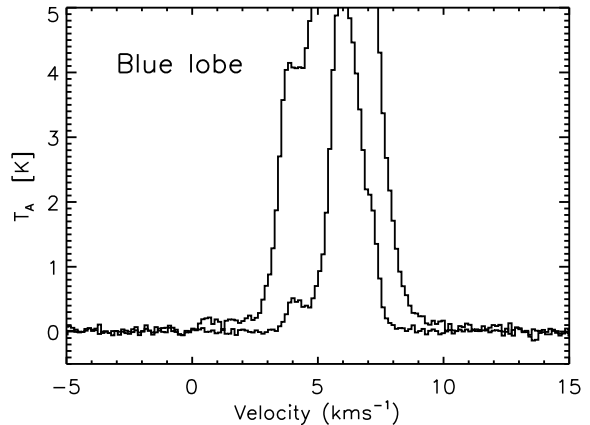


FIG. 7.—  $^{12}\text{CO}$  (thick) and  $^{13}\text{CO}$  (thin) spectra averaged in the blueshifted lobe of the Haro 6-10 outflow.

contaminating component and enhanced outflow wings. The outflow in  $^{12}\text{CO}$  can be traced over a full velocity range from 0 to 14  $\text{km s}^{-1}$ .

Despite this averaging approach, the  $^{13}\text{CO}$  emission outside the line cores, has low signal to noise. Examining both Figures 6 and 7 we see that at the full spectral resolution, the  $^{13}\text{CO}$  emission is lost in noise at velocities below than 2  $\text{km s}^{-1}$  and greater than 9  $\text{km s}^{-1}$ . The  $^{13}\text{CO}$  outflow emission is too weak to use velocity-dependent opacity correction. We have instead integrated the emission in four velocity intervals. In the near-wings of the redshifted outflow emission (between 8 and 9  $\text{km s}^{-1}$ ) the ratio of  $^{12}\text{CO}$  to  $^{13}\text{CO}$  is  $112 \pm 20$ , consistent with the  $^{12}\text{CO}$  emission being optically thin. At higher outflow velocities (between 9 and 12  $\text{km s}^{-1}$ ),  $^{13}\text{CO}$  emission is not detected, and the  $1\sigma$  lower limit on this ratio is 47. The  $^{13}\text{CO}$  emission in the blueshifted gas is even weaker, and only limits on the ratio can be obtained. In the near blueshifted outflow (2 to 3  $\text{km s}^{-1}$ ) the  $1\sigma$  lower limit is 45 and at higher blueshifted velocities (0 to 2  $\text{km s}^{-1}$ ) the lower limit is 20. Thus, where  $^{13}\text{CO}$  emission is detected it is consistent with optically thin  $^{12}\text{CO}$  emission and everywhere else we can only determine an upper limit to the  $^{12}\text{CO}$  optical depth. Therefore to estimate the gas column density and outflow mass, we will assume that  $^{12}\text{CO}$  emission is optically thin (equation 3 from Stojimirović et al. (2006)), and we will apply no correction for the optical depth.

The outflow mass as a function of velocity and position is then computed from  $M(v) = 2\mu m_H A N_{H_2}(v)$ , where  $\mu = 1.36$  is the mean atomic weight including He and other constituents,  $m_H$  is the mass of the hydrogen atom and  $A$  is the physical area of one pixel at the distance of the source.  $N_{H_2}$  is the molecular hydrogen column density obtained using the relation  $N_{H_2} = 1.1 \times 10^4 N_{12}$  by Frerking et al. (1982) for the Taurus cloud; this result is consistent with more recent determinations, summarized by Harjunpää et al. (2004), for other nearby dark clouds. The greatest uncertainty in our mass estimates comes from the uncertainty in the  $N_{H_2}$  to  $N_{12}$  ratio (Frerking et al. 1982).

The gas column density derived assuming that CO is in LTE depends on the gas temperature. For a gas temperature of 10 K we find  $0.02 M_\odot$  in the velocity range from

TABLE 1  
OUTFLOW MASS ESTIMATES

Velocity Interval	$T_{\text{ex}} = 10 \text{ K}$	$T_{\text{ex}} = 25 \text{ K}$
	Mass $M_{\odot}$	Mass $M_{\odot}$
Red 8 to 9 $\text{km s}^{-1}$	0.1	0.15
Red 9 to 14 $\text{km s}^{-1}$	0.02	0.03
Blue 0 to 2 $\text{km s}^{-1}$	0.01	0.02
Blue 2 to 3 $\text{km s}^{-1}$	0.02	0.04
Red Total	0.12	0.18
Blue Total	0.03	0.06

9 to 14  $\text{km s}^{-1}$ , while the mass in the velocity range from 0 to 2  $\text{km s}^{-1}$  is found to be 0.01  $M_{\odot}$ . For a gas temperature of 25 K, in the same velocity ranges, the redshifted gas has mass of 0.04  $M_{\odot}$  and blueshifted of 0.02  $M_{\odot}$ . We believe that these velocity ranges are dominated by outflow emission.

The cutoff velocity of 9  $\text{km s}^{-1}$  for the start of the redshifted component of the outflow and 2  $\text{km s}^{-1}$  for the start of the blueshifted component correspond to velocity offsets from the systemic velocity of the cloud of 2.5 and 4.5  $\text{km s}^{-1}$ , respectively. There is likely slower-moving gas at lower redshifted and blueshifted velocities that is missed in our analysis. Within the blueshifted velocities, the presence of the contaminating emission at 4.5  $\text{km s}^{-1}$  clearly makes it problematic to single out the low-velocity outflow component. Our outflow mass estimates are therefore lower limits. In an effort to include any lower-velocity outflow gas, we have repeated the mass calculation for the redshifted velocity range of 8 to 9  $\text{km s}^{-1}$  and derive a mass of 0.15  $M_{\odot}$ , and for the blueshifted velocity range of 2 to 3  $\text{km s}^{-1}$  and derive a mass of 0.04  $M_{\odot}$ , both assuming a gas temperature of 25 K. Our mass estimates are summarized in Table 1.

The mass distribution with velocity for molecular outflow has been shown to have a power-law dependence, such that  $M(v) \propto v^{-\gamma}$  (Richer et al. 2000). We have derived the mass-velocity relation for Haro 6-10 using the  $^{12}\text{CO}$  emission and assuming it is optically thin as we assumed earlier. We computed the mass in each velocity channel within the outflow and plotted this versus the velocity offset from the host cloud's mean velocity. The velocity range over which outflow gas is detected in Haro 6-10 is very limited, making the determination of this relation very uncertain. In a log-log plot, the slope of the linear fit determines the  $\gamma$  index. The value of  $\gamma$  for the blueshifted gas is  $6 \pm 0.6$  and for the redshifted gas is  $5.5 \pm 0.6$ .

#### 4.2. Cloud Mass and Energy

We determine the cloud mass by using the  $^{13}\text{CO}$  map, Figure 3b. The line center optical depth at each point in the map is derived from the  $^{13}\text{CO}$  peak temperature. The excitation temperature is obtained at each position by solving the radiative transfer equation for the excitation temperature, assuming  $^{12}\text{CO}$  line to be optically thick. We find, the total mass of the cloud using this method to be  $\sim 200 M_{\odot}$ . The cloud mass estimate is mostly free from the foreground contamination, since we only searched for peak  $^{13}\text{CO}$  emission in the narrow velocity

range around line center.

The kinetic energy of the cloud is dominated by the turbulent energy of the cloud, and is estimated using  $E_{\text{turb}} = 3/(16\ln 2)M_{\text{cloud}}\Delta v^2$ . The mean turbulent velocity of the ambient gas is determined from the  $^{13}\text{CO}$  line profiles in the cloud. We find the full line width at the half maximum to be  $\Delta v = 1.2 \text{ km s}^{-1}$ . We find that kinetic energy of the L 1524 cloud is  $\sim 1.6 \times 10^{45}$  ergs.

#### 5. DISCUSSION

Although at the lowest outflow velocities, the blueshifted emission is strongly contaminated by the foreground cloud emission, we see signatures of the outflow from Haro 6-10 at the higher blueshifted velocities. There is significant overlap between blueshifted and redshifted emission at the position of Haro 6-10, which together with relatively low velocities observed in the line wings, suggests that the flow is in the plane of the sky. If the flow is in the plane of sky, slower radial velocities are hidden under the ambient cloud emission. In such a scenario, the clumps that we see defined in the redshifted gas (see for instance Figure 5) are probably the highest velocity components seen projected in the map.

A position-velocity (P-V) cut along the axis of the HH flow is shown in Figure 8. High velocity emission is seen at the location of Haro 6-10 (at offset 0 in the P-V plot) and at the position of HH 412 (at offset 6.3). The highest velocity red-shifted emission is associated with HH 412. The P-V plot also reveals a general broadening of the CO emission at redshifted velocities between offsets of 0 and  $+20'$ , and at blueshifted velocities between offsets of 0 and  $-10'$ . The broadening at these positions is not symmetric about the cloud's systemic velocity, but rather, is wider at redshifted velocities for positive offsets and at blueshifted velocities for negative offsets. The positive and negative positional offsets in Figure 8 correspond to the location of redshifted and blueshifted lobes respectively of the overall Haro 6-10 outflow system. The slight broadening at positive and negative offsets in the PV plot further bolsters the argument that the Haro 6-10 molecular outflow is, at least in the current epoch, a very low-velocity outflow that has slowed down close to ambient cloud velocities. If this is correct, it may be possible to see the subtle signature of the outflow at low velocities from constructing a centroid velocity map with velocities confined to the ambient cloud emission alone (6 to 7  $\text{km s}^{-1}$ ). When such centroid velocity mapping was performed, for instance in the Cepheus A outflow system (see Figure 4 of Narayanan & Walker 1996), it was found that the outflow signature is clearly seen as a velocity gradient along the outflow direction. We have performed such centroid velocity mapping analysis (figure not shown) for Haro 6-10, but we do not see any such gradient present at ambient cloud velocities. This leads us to conclude that even if the outflow has slowed to ambient cloud velocities in Haro 6-10, the outflow has not imparted any significant velocity gradients over the normally present random velocities inherent in the ambient cloud.

Yet another puzzling feature of the Haro 6-10 outflow is, that it entrains very little gas. The morphology of the outflow is very clumpy and the total mass found in the outflow is only 0.25  $M_{\odot}$ . In evolved sources, the previous outflow episodes may clear up the ambient gas and

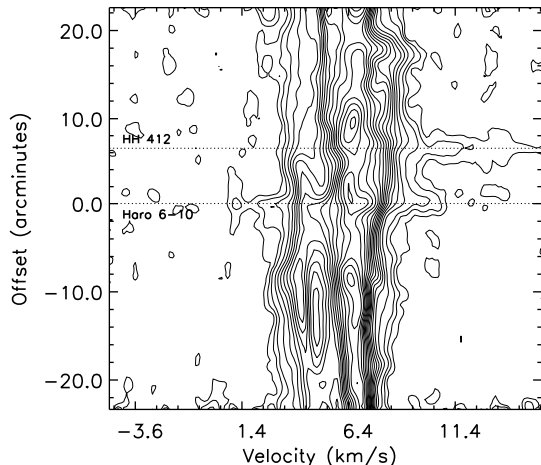


FIG. 8.— Position-Velocity cut for the Haro 6-10 outflow, along the axis defined by the parsec-scale HH flow, position angle  $40^\circ$ . Haro 6-10 is located at an offset position of 0, and HH 412 is located at offset position of  $+6.3'$ . The cut is wide 5 pixels, which corresponds to  $\sim 2'$ .

leave no gas to be entrained by later outflow episodes. In such a case, large ambient gas cavities are expected to be seen around source. Our  $^{13}\text{CO}$  maps show that no such cavities are found around Haro 6-10 and that the overall L 1524 cloud is somewhat flattened and filamentary, with the column density decreasing from Haro 6-10 source toward HH 410 and HH 411 along the outflow axis. While the L 1524 cloud is flattened, there appears to be enough ambient gas in the direction of the outflow lobes to be entrained (see Figure 3).

The clumpy morphology and low total mass may be a consequence of the outflow viewing geometry. If the outflow is mostly in the plane of sky, much of its mass would be missed since we have excluded ambient gas components from our calculations. It would be interesting to obtain proper motion study of the HH knots to determine the orientation of the flow with respect to the plane of the sky.

The outflow emission beyond Haro 6-10 is strictly confined to the HH 412 knot and it has the same elongated morphology as its optical counterpart. Therefore they seem to be created by the same mechanism. The HH knots are formed where the fast jet is interacting with the ambient gas. They can be found at the head of the jet or along its body at the locations of internal working surfaces where the new ejecta is catching up with the previously ejected slow-down gas. The CO clump at HH 412 is detached from the Haro 6-10 source. It has small mass, and it is detected up to the projected velocities of  $8 \text{ km s}^{-1}$  from the line center.

Due to various contaminations, we had to use velocities far from the line core to study the mass distribution in the case of Haro 6-10. This could be another reason why there is so little mass recovered in the outflow. Observational studies show that outflows show a power law distribution of the mass with respect to the velocity offset from the cloud velocity. This distribution is such that most of the outflow mass is at low velocities. The first mass point that we account for, in Haro 6-10 outflow, is offset by  $2.6 \text{ km s}^{-1}$  from the line center. For the  $V_{LSR}$  of  $6.4 \text{ km s}^{-1}$  we calculated the outflow mass only for the

points between  $9\text{-}14 \text{ km s}^{-1}$  and  $0$  to  $2 \text{ km s}^{-1}$ . Therefore we may be missing a significant fraction of the mass as it is increasing with the decreasing outflow velocity, and the estimated outflow masses are consequently lower limit.

Lastly, we can compare Haro 6-10 outflow to the HH 300 parsec scale flow in the nearby B 18w cloud, studied by AG. AG found that the HH 300 outflow has a very clumpy structure and they identified five  $^{12}\text{CO}$  redshifted clumps with masses from  $0.03$  to  $0.23 M_\odot$  and radial velocities of about  $3 \text{ km s}^{-1}$  from the ambient cloud velocity. They also noted that the clumps have different position angles with respect to the driving source and concluded that the flow most likely precess with each clump corresponding to the different ejection event. The similarity of the HH 300 and Haro 6-10 outflow in terms of clumpy morphology and mass content is apparent. However while the redshifted clumps of HH 300 flow are found at different position angles with respect to the IRAS source the redshifted clump at HH 412 location in Haro 6-10 flow is found elongated along the jet (as is HH 412) axis defined by HH flow. Although there are evidence that the current jet axis from the Haro 6-10 differs from the axis defined by the parsec scale flow (Reipurth et al. 2004; Devine et al. 1999; Movsessian & Magakian 1999), the jet in Haro 6-10 must have had a stable orientation for a long time since all HH knots in the Haro 6-10 outflow which are found at large distance from the source (HH 410, 411, & 412) as well as the HH 184E, lie on the  $222^\circ$  position angle jet axis. The HH 300 outflow exhibits larger impact on its host cloud, with  $^{13}\text{CO}$  line showing bipolar structure of the cloud gas at velocities close to the line center. Surprisingly, Haro 6-10 outflow does not seem to be affecting its host cloud's kinematics significantly.

AG find a steep broken power law in the mass-velocity distribution with  $\gamma = 4.0$  at low outflow velocities and  $\gamma = 7.8$  for outflow velocities greater than  $1.85 \text{ km s}^{-1}$ . We find the slope  $\gamma$  in the mass-velocity distribution of the Haro 6-10 outflows to be around  $\sim 6$ . This value is much steeper than the average of  $\gamma \sim 2$  reported for a collection of outflow sources (Richer et al. 2000). The steepening of the  $\gamma$  index is expected for the older outflows, where once accelerated ambient material will slow down leading to accumulation of slow material. It is worth noting that the break in the mass-velocity distribution in the nearby HH 300 outflow happens very close to the line core. If the same holds for the Haro 6-10 we may be missing the shallower part at low velocities since we only account for the mass at velocities which have offset of at least  $2.5 \text{ km s}^{-1}$  (toward redshifted) and  $4.5 \text{ km s}^{-1}$  (toward blueshifted) from the systemic velocity of the cloud. The broken power law is usually a good indicator of the jet entrainment model (Zhang & Zheng 1997).

## 6. SUMMARY AND CONCLUSIONS

We made large, sensitive,  $^{12}\text{CO}$   $J=1\rightarrow 0$  and  $^{13}\text{CO}$   $J=1\rightarrow 0$  maps of the Haro 6-10 region, over the full extent of the optical parsec-scale HH flow. Here we summarize our main conclusions:

1. The redshifted outflow component is clearly detected emerging from Haro 6-10 toward northeast, along the axis of optically defined parsec-scale HH flow.

2. Contamination from an unrelated foreground cloud along the same line of sight prevents a thorough study of the blueshifted outflow lobe, which we detect centered on Haro 6-10 in the opposite direction from redshifted lobe, and in the velocity range from 0 to 2 km s<sup>-1</sup>.
3. The mass and energies of the outflow are significantly smaller than those of the host molecular cloud. However, most of the mass might be missed due to an unrelated contamination at lower outflow velocities, along the same line of sight, and/or in the plane of the sky orientation of the outflow.
4. In the optical maps next to the HH 412, Haro 6-10 parsec scale flow is crossed by HH 414/413 flow. In CO data at the lowest redshifted velocities, there seem to be evidence of HH 414 IRS activity toward HH 413.

This work was supported by NSF grant AST 02-28993 to the Five College Radio Astronomy Observatory.  
Facilities: FCRAO

## REFERENCES

- Arce, H. G. & Goodman, A. A. 2001a, *ApJ*, 554, 132  
 Bachiller, R., Guilloteau, S., Dutrey, A., Planesas, P., & Martin-Pintado, J. 1995, *A&A*, 299, 857  
 Bally, J., Reipurth, B., Lada, C. J., & Billawala, Y. 1999, *AJ*, 117, 410  
 Chandler, C. J., Barsony, M., & Moore, T. J. T. 1998, *MNRAS*, 299, 789  
 Carr, J. S. 1990, *AJ*, 100, 1244  
 Codella, C., Welser, R., Henkel, C., Benson, P. J., & Myers, P. C. 1997, *A&A*, 324, 203  
 Devine, D., Reipurth, B., Bally, J., & Balonek, T. J. 1999, *AJ*, 117, 2931  
 Edwards, S., & Snell, R. L. 1984, *ApJ*, 281, 237  
 Frerking, M. A., Langer, W. D., & Wilson, R. W. 1982, *ApJ*, 262, 590  
 Harjunpää, P., Lehtinen, K., & Haikala, L. K. 2004, *A&A*, 421, 1087  
 Herbst, T. M., Koresko, C. D., & Leinert, C. 1995, *ApJ*, 444, L93  
 Heyer, M. H., Snell, R. L., Goldsmith, P. F., & Myers, P. C. 1987, *ApJ*, 321, 370  
 Hogerheijde, M. R., van Dishoeck, E. F., Blake, G. A., & van Langevelde, H. J. 1997, *ApJ*, 489, 293  
 Hogerheijde, M. R., van Dishoeck, E. F., Blake, G. A., & van Langevelde, H. J. 1998, *ApJ*, 502, 315  
 Langer, W. D. & Penzias, A. A. 1993, *ApJ*, 408, 539  
 Lee, C., Mundy, L. G., Reipurth, B., Ostriker, E. C., & Stone, J. M. 2000, *ApJ*, 542, 925  
 Lee, C.-F., Stone, J. M., Ostriker, E. C., & Mundy, L. G. 2001, *ApJ*, 557, 429  
 Lee, C.-F., Mundy, L. G., Stone, J. M., & Ostriker, E. C. 2002, *ApJ*, 576, 294  
 Levreault, R. M. 1988, *ApJ*, 330, 897  
 Masson, C. R., & Chernin, L. M. 1993, *ApJ*, 414, 230  
 Matzner, C. D. & McKee, C. F. 1999, *ApJ*, 526, L109  
 Movsessian, T. A., & Magakian, T. Y. 1999, *A&A*, 347, 266  
 Narayanan, G., & Walker, C. K. 1996, *ApJ*, 466, 844  
 Narayanan, G., Heyer, M. H., Brunt, C., Goldsmith, P. F., Snell, R., Tang, Y., and Li, D., 2007, in preparation  
 Reipurth, B., Bally, J., & Devine, D. 1997, *AJ*, 114, 2708  
 Reipurth, B., Rodríguez, L. F., Anglada, G., & Bally, J. 2004, *AJ*, 127, 1736  
 Richer, J. S., Shepherd, D. S., Cabrit, S., Bachiller, R., & Churchwell, E. 2000, *Protostars and Planets IV*, 867  
 Shu, F. H., Laughlin, G., Lizano, S., & Galli, D. 2000, *ApJ*, 535, 190  
 Stahler, S., 1994, *ApJ*, 422, 616  
 Stojimirović, I., Narayanan, G., Snell, R. L., & Bally, J. 2006, *ApJ*, 649, 280  
 Yu, K., Billawala, Y., & Bally, J. 1999, *AJ*, 118, 2940  
 Yu, K. C., Billawala, Y., Smith, M. D., Bally, J., & Butner, H. M. 2000, *AJ*, 120, 1974  
 Zhang, Q. & Zheng, X. 1997, *ApJ*, 474, 719

This figure "f2.jpg" is available in "jpg" format from:

<http://arXiv.org/ps/astro-ph/0702273v1>

This figure "f5.jpg" is available in "jpg" format from:

<http://arXiv.org/ps/astro-ph/0702273v1>